Supplementary Materials on

Large thermoelectric effect driven by high-order anharmonicity from synergistic lone-pair electrons and rattling modes in $K_3Au_3Sb_2$

Yibo Gao, Ting Zhao, Min Li and Hui Wang*

School of Physics, Hunan Key Laboratory of Super Microstructure and Ultrafast Process, Hunan Key Laboratory of Nanophotonics and Devices, State Key Laboratory of Powder Metallurgy, Central South University, Changsha 410083, China

Section S1. Details of carrier transport property calculations

In this work, the electronic scattering rates based on Fermi golden rule were performed with ab initio scattering and transport (AMSET) [1] code. The elastic scattering rate was described as:

$$\tau_{i\mathbf{k}\to j\mathbf{k+q}}^{-1}=\frac{2\pi}{\hbar}\langle j\mathbf{k+q}|g_{ij}|i\mathbf{k}\rangle^2\delta(E_{i\mathbf{k}}-E_{j\mathbf{k+q}}) \tag{S1}$$

and the inelastic scattering rate was:

$$\begin{aligned}\tau_{i\mathbf{k}\to j\mathbf{k+q}}^{-1}=\frac{2\pi}{\hbar}\langle j\mathbf{k+q}|g_{ij}|i\mathbf{k}\rangle^2[(n_{\mathbf{q}}+1-f^{0}_{j\mathbf{k+q}})\delta \\ (E_{i\mathbf{k}}-E_{j\mathbf{k+q}}-\hbar\omega_{\mathbf{q}})+(n_{\mathbf{q}}+f^{0}_{j\mathbf{k+q}})\delta(E_{i\mathbf{k}}-E_{j\mathbf{k+q}}+\hbar\omega_{\mathbf{q}})]\end{aligned} \tag{S2}$$

where$i\mathbf{k}$represents the initial state of the$\boldsymbol{i}$-th electron, and the $\boldsymbol{i}$ and $\mathbf{k}$ are the band index and electron wave vector, respectively. $j\mathbf{k+q}$ denotes the final state within the Born approximation when the electron initial state $i\mathbf{k}$couples with the phonon with wave vector$\mathbf{q}$ and frequency $\omega_{\mathbf{q}}$. The δ, n, and f mean the Dirac delta function, the Bose-Einstein distribution, and the Fermi-Dirac distribution, respectively. $-\hbar\omega_{\mathbf{q}}$ and $+\hbar\omega_{\mathbf{q}}$ refer to the energy changes associated with the absorption and emission of a phonon, respectively. Consequently, the electronic scattering rates were evaluated in consideration of the elastic acoustic deformation potential (ADP) scattering, the ionized impurity (IMP) scattering and the inelastic polar optical phonon (POP) scattering. To systematically evaluate the impact of spin-orbit coupling, the fundamental band structures and wave function coefficients used as inputs were derived from both PBE and PBE+SOC calculations. Specifically, both the ADP and POP scattering mechanisms are treated within the long-wavelength limit, utilizing macroscopic parameters and phonon frequencies exclusively at the Brillouin zone center(Γ -point). We explicitly acknowledge the study limitation that the electron-phonon interactions in this framework rely on the Γ-point approximation rather than a full-Brillouin-zone integration. Despite this limitation, the AMSET code effectively mitigates this approximation by rigorously integrating the exact scattering phase space derived from the full-Brillouin-zone DFT band structures. The accuracy of this sophisticated treatment has been extensively validated in various reported thermoelectric (TE) materials (e.g., GeSe, SnSe, $PbSnSe_2$, and $SrSnSe_2$) [1–4],

yielding results comparable to those obtained by the state-of-the-art EPW code. Therefore, the calculated carrier relaxation times in this work are highly reliable, providing robust and accurate theoretical predictions for the $K_3Au_3Sb_2$ system.

Section S2. Explanation of Regular Residual Analysis

The standard Taylor series expansion $f(x)$:

$$f(x)=f(0)+\frac{1}{1!}f'(0)x+\frac{1}{2!}f''(0)x^2+\frac{1}{3!}f'''(0)x^3+\frac{1}{4!}f^{(4)}(0)x^4+\cdots \quad \text{(S3)}$$

where x is the small perturbation around 0. To deal with actual physical problems, the equation can be transformed into a polynomial function $F(x)$:

$$F(x)=ax^2-bx^3+cx^4+O(x^5) \quad \text{(S4)}$$

where a, b, and c are the coefficients of the second-, third-, and fourth-order terms, respectively, and $O(x^5)$ is the sum of higher-order terms. For lattice vibrations, the second-order terms represent harmonic vibrations, whereas the higher-order terms correspond to anharmonic vibrations. The Relative Regular Residual (RRR) is thus mathematically defined as the relative difference between the actual ab initio potential energy values (F_{total}) and the predicted harmonic values ($F_{harmonic}$):

$$RRR=F_{total}(x)-F_{harmonic}(x)\approx -bx^3+cx^4 \quad \text{(S5)}$$

The shape of the resulting RRR curve provides a direct visual and mathematical metric for the strength of the intrinsic fourth-order anharmonicity [4,5]:

- Weak Fourth-Order Anharmonicity: When the fourth-order coefficient (c) is negligible compared to the third-order term, the RRR curve is dominated by the cubic term ($-bx^3$), typically presenting a "~"-like shape.
- Strong Fourth-Order Anharmonicity: Conversely, when the absolute value of the fourth-order coefficient (c) is significantly large, the quartic term (cx^4) dominates at larger displacements. The RRR curve transitions into a fourth-polynomial behavior, presenting a distinct "W"-like shape (or "M"-like, depending on the sign).

Section S3. Supplementary Data

Table S1. *Comparison of experimental and calculated lattice parameters (a, b, c) for* $K_3Au_3Sb_2$.

Lattice parameter	a	b	c
Experimental	6.20Å	6.20Å	21.52Å
Calculation	6.36Å	6.36Å	21.82Å

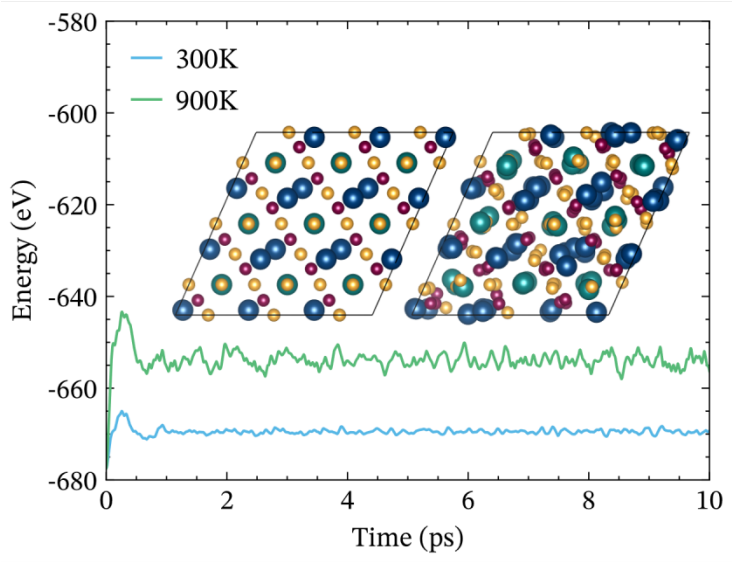

Fig S1. *Ab initio molecular dynamics (AIMD) simulations of* $K_3Au_3Sb_2$ *performed at 300 K and 900 K. The vertical axis denotes the system potential energy, and the horizontal axis represents the simulation time.*

The main panel displays the evolution of potential energy over a 10 ps simulation period. The insets show the ideal crystal structure at the beginning (left) and the structural snapshot at the end (right) of the 900 K simulation. The steady potential energy oscillations around an equilibrium value, coupled with the maintained structural integrity without any signs of lattice collapse, confirm the excellent thermal stability of the system up to 900 K.

Table S2. *Electronegativity, valence electrons (Z_{val}), Bader charge (Q_B), and net charge (Q_{net}) of each atom in $K_3Au_3Sb_2$*

Element	Electronegativity	Z_{val}	Q_B	Q_{net}	Charge Status
Sb	2.05	5	4.85	+0.15	Near-neutral
K	0.82	9	8.44	+0.56	Electron Donor
Au	2.54	11	11.66	-0.66	Electron Acceptor

To elucidate the charge transfer mechanism within the system, Bader charge analysis was performed (Table S2). The results demonstrate that the direction of charge transfer is strictly governed by the electronegativity differences among the constituent elements. Potassium (K), possessing the lowest electronegativity (0.82), acts as a typical electron donor, losing electrons to exhibit a net charge of +0.56 e^-Conversely, the covalent polyanionic framework composed of Au and Sb serves as the electron acceptor. Notably, because the electronegativity of Au (2.54) is significantly higher than that of Sb (2.05), Au exhibits a strong electron-withdrawing capability and becomes the primary target for electron transfer (net charge of -0.66 e^-), while Sb remains in a near-neutral state (net charge of+0.15 e^-). This pronounced charge transfer from the electropositive alkali metal to the $[Au_3Sb_2]^{3-}$ anionic framework and specifically to the highly electronegative Au atoms—perfectly corroborates the hierarchical bonding character typical of Zintl phases.

Based on the aforementioned Bader charge results, we further justify the physical rationale for omitting the Hubbard U correction (DFT+U) in this work. Primarily, the fundamental prerequisite for introducing the U parameter is to correct for the strong electron correlation effects present in partially filled and highly localized d or f orbitals (such as those in 3d transition metals) [6]. However, Au is a heavy transition metal whose 5d orbitals possess a large spatial radial extent, leading to a higher degree of electron delocalization and inherently weak on-site Coulomb repulsion. More importantly, as indicated by the Bader data, Au acts as an electron acceptor in this system and adopts a distinct negative valence state. This signifies that its 5d orbitals are in a fully occupied, closed-shell state (d^{10} electron configuration). Such fully occupied and spatially extended d-orbital characteristics contradict the physical prerequisites required for the +U correction. Therefore, the standard GGA-PBE functional is sufficiently accurate to describe the intrinsic electronic structure of this

system. This methodological choice is entirely consistent with the computational parameters adopted in classic literature of the field, such as (etc., AuS_2, AuNi) [7,8].

Table S3. *Integrated Crystal Orbital Hamilton Population (-ICOHP) values for each atom pair in $K_3Au_3Sb_2$.*

Atom Pair	Sb-Au	Sb-K1	Sb-K2	Au-K1	Au-K2	K1-K2
-ICOHP	1.61	0.29	0.16	0.11	0.06	0.21

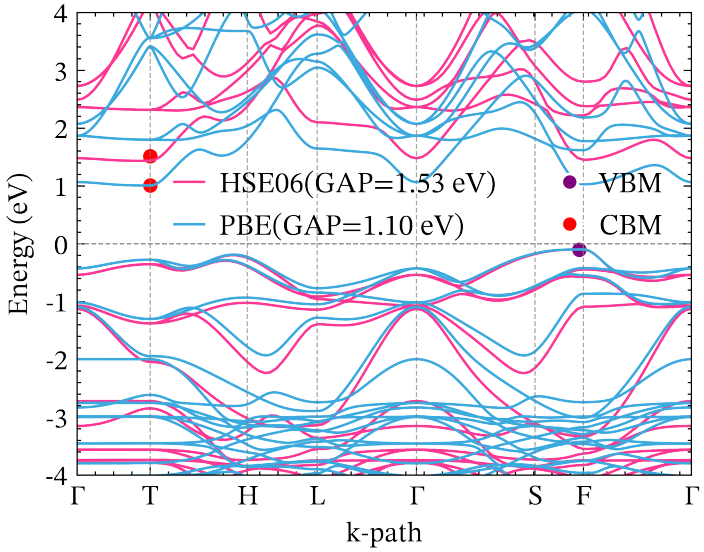

Fig S2. *Calculated band structures of $K_3Au_3Sb_2$ using PBE (blue) and HSE06 (pink) functionals.*

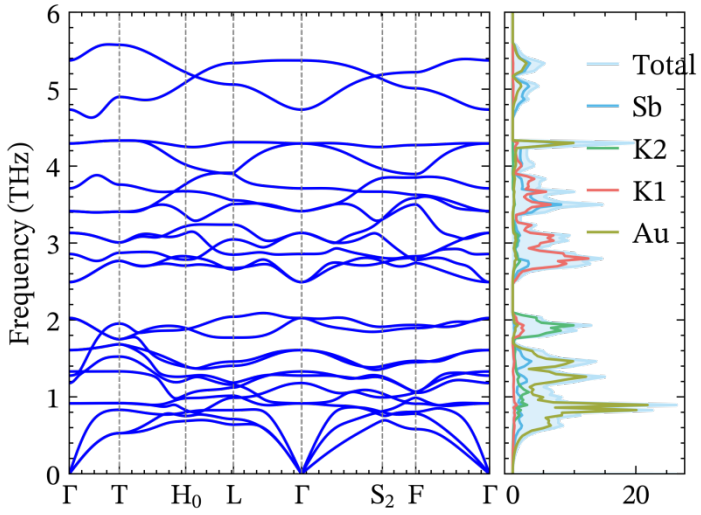

Figure S3. *Calculated phonon dispersion relations (left panel) and the corresponding phonon density of states (right panel).*

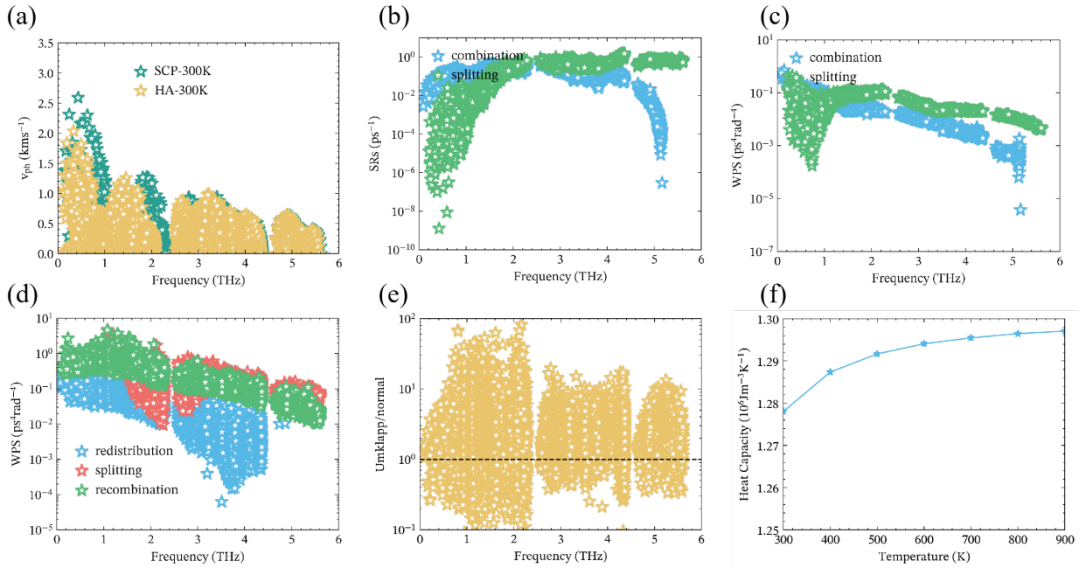

Fig. S4. *(a) Phonon group velocity of HA and SCP (b) Three-phonon scattering: combination and splitting processes. (c) Three-phonon scattering channels: combination and splitting processes. (d) Four-phonon scattering channels: redistribution, splitting, and recombination processes. (e) Ratio of Umklapp to Normal processes for four-phonon scattering. (f) Heat capacity as a function of temperature.*

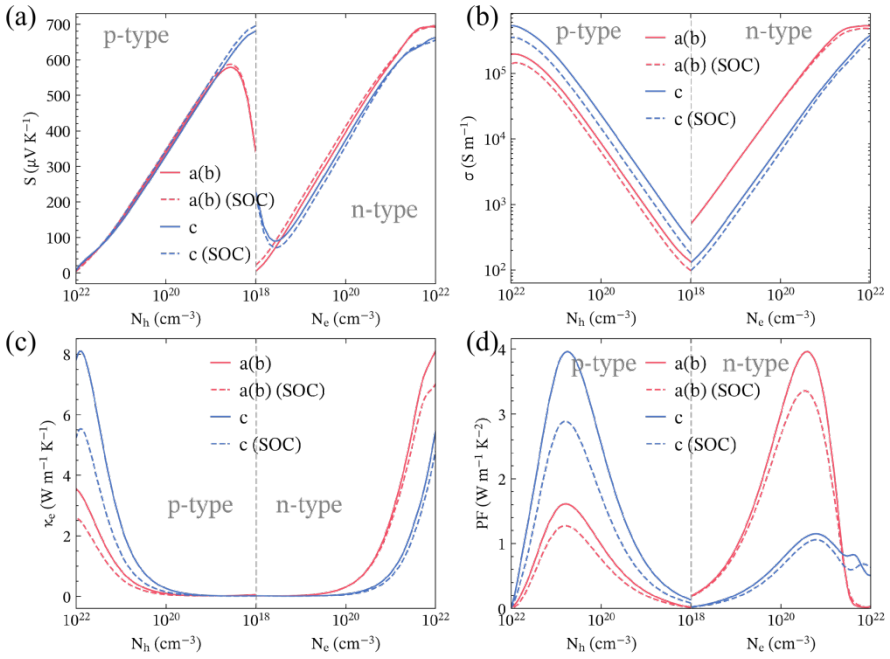

Fig. S5. *Electrical transport properties at 900 K: (a) Seebeck coefficient S, (b) electrical conductivity σ, (c) electronic thermal conductivity κ_e, and (d) power factor PF versus carrier concentration for p-type (N_h) and n-type (N_e) doping, comparing directions a(b) and c with (dashed) and without (solid) spin-orbit coupling.*

Reference

[1] A. M. Ganose, J. Park, A. Faghaninia, R. Woods-Robinson, K. A. Persson, and A. Jain, Efficient calculation of carrier scattering rates from first principles, Nature Communications **12**, 2222 (2021).

[2] A. D. Becke and E. R. Johnson, A simple effective potential for exchange, Journal of Chemical Physics **124**, 221101 (2006).

[3] M. Zhang, J. M. Flitcroft, S. K. Guillemot, and J. M. Skelton, Thermoelectric properties of *Pnma* and *R*3*m* GeS and GeSe, Journal of Materials Chemistry C **11**, 14833 (2023).

[4] S. Bai et al., Revealing the origin of anisotropic Rashba spin-orbital splitting and four-phonon scattering in strontium-tin-selenium thermoelectrics, Advanced Functional Materials **35**, 2414288 (2025).

[5] S.-Y. Yue, X. Zhang, G. Qin, S. R. Phillpot, and M. Hu, Metric for strong intrinsic fourth-order phonon anharmonicity, Physical Review B **95**, 195203 (2017).

[6] S. L. Dudarev, G. A. Botton, S. Y. Savrasov, C. J. Humphreys, and A. P. Sutton, Electron-energy-loss spectra and the structural stability of nickel oxide: An LSDA+U study, Physical Review B **57**, 1505 (1998).

[7] F. Garmroudi, M. Parzer, A. Riss, C. Bourgès, S. Khmelevskyi, T. Mori, E. Bauer, and A. Pustogow, High thermoelectric performance in metallic NiAu alloys via interband scattering, Science Advances **9**, eadj1611 (2023).

[8] W. Zhang, X.-Q. Zhang, L. Liu, Z.-Q. Wang, and Z.-G. Li, Two-dimensional square-Au_2S monolayer: A promising thermoelectric material with ultralow lattice thermal conductivity and high power factor, Chinese Physics B **30**, 077405 (2021).